Published in final edited form as:
Appl Spectrosc. 2009 July ; 63(7): 759–766. doi:10.1366/000370209788701044.

Attenuated Total Internal Reflectance Infrared Spectroscopy (ATR-FTIR): A Quantitative Approach for Kidney Stone Analysis

Heather J. Gulley-Stahl, **Jennifer A. Haas**, **Katherine A. Schmidt**, **Andrew P. Evan**, and **André J. Sommer**
Molecular Microspectroscopy Laboratory, Department of Chemistry and Biochemistry, Miami University, Oxford, OH 45056, USA; Department of Anatomy and Cell Biology, Indiana University School of Medicine, Indianapolis, IN 46202, USA

Abstract

The impact of kidney stone disease is significant worldwide, yet methods for quantifying stone components remain limited. A new approach requiring minimal sample preparation for the quantitative analysis of kidney stone components has been investigated utilizing attenuated total internal reflectance infrared spectroscopy (ATR-FTIR). Calcium oxalate monohydrate (COM) and hydroxylapatite (HAP), two of the most common constituents of urinary stones, were used for quantitative analysis. Calibration curves were constructed using integrated band intensities of four infrared absorptions versus concentration (weight %). The correlation coefficients of the calibration curves range from 0.997 to 0.93. The limits of detection range from 0.07 ± 0.02% COM/HAP where COM is the analyte and HAP the matrix to 0.26 ± 0.07% HAP/COM where HAP is the analyte and COM the matrix. This study shows that linear calibration curves can be generated for the quantitative analysis of stone mixtures provided the system is well understood especially with respect to particle size.

Index Headings

Quantitative ATR-FTIR; Kidney stones; Calcium oxalate monohydrate; Hydroxylapatite

Introduction

Urolithiasis, or kidney stone disease, is common throughout the world and affects approximately 10% of the United States population. The incidence of urolithiasis has seen a dramatic increase worldwide in the last twenty years.[1,2] Limited data exists outlining the complete current economic impact of urolithiasis in the United States, but in 2005 the total annual cost for urolithiasis treatment in the US was estimated to be $2 billion.[3,4] Kidney stones are recurrent in about 60% of patients while 10% are afflicted by multi-recurrent nephrolithiasis disease. For stone formers, treatment can be painful, stone removal often requires surgery, and about 3% of patients experience renal failure as a result of nephrolithiasis.[5] Due to the complex nature of urine, kidney stones are typically composed of multiple organic and inorganic constituents which can vary from calcium oxalate hydrates, calcium phosphates, proteins, etc. Calcium oxalates, including calcium oxalate monohydrate (COM), are the most frequent constituents in urinary stones, appearing about 80% of the time, and hydroxylapatite (HAP) is the second most prevalent, appearing in about 12% of stones.[6–10]

The exact mechanism of kidney stone formation has yet to be totally resolved. With proper methods, the analysis of biopsied tissue from kidney stone formers can allow the identification of small mineral inclusions during the initial stages of stone formation.[11] This

laboratory is currently focused on the analysis of biopsied tissue removed from idiopathic calcium stone formers. Idiopathic calcium stone formers typically produce calcium oxalate stones which are characterized by an initial formation of Randall's plaque. Because Randall's plaque is predominately composed of HAP, mixed stone inclusions of COM and HAP are very common.[12–14] Performing quantitative analysis to determine the amount of COM or HAP at the localized stone/tissue interface could potentially allow a better understanding of initial stone formation.

Current methods for quantifying kidney stone components are lacking. While urolithiasis treatment can depend on stone composition, approximately 30% of stones are misdiagnosed due to the qualitative wet chemical analysis commonly used, including commercial kits.[2] As urinary stone components become mixed, the incidence of misdiagnoses increases. Current analytical techniques for the qualitative and quantitative analysis of urinary stones include infrared spectroscopy (IR), wet chemical analysis, thermogravimetry, x-ray diffraction (XRD), and scanning electron microscopy (SEM) with energy dispersive X-ray.[2,15–19] XRD and IR provide the most reliable results, but remain qualitative in nature and may require destruction of the stone sample.

Previous studies have employed FTIR in a quantitative study for kidney stone analysis, but this approach requires extensive sample preparation and utilizes nonlinear calibration curves.[6,20,21] In 2004, Cohen-Solal et al. generated calibration curves for the quantitative analysis of calcium oxalate dihydrate (COD) and carbapatite (CA). Because biological stone samples were utilized, only a small amount of sample was available. Therefore, the calibration curves reported consist of only three experimental data points at 30, 50 and 70 wt % CA.[20] Ultimately, the calibration curves developed by Cohen-Solal were software produced polynomial curves with computer generated points at every 5 wt %. The authors fail to discuss why a polynomial fit was utilized as opposed to a linear fit, but do state that the particle sizes of powdered samples makes quantitative analysis difficult when using a transmission IR sampling method. Estepa et al. of the same group also reported nonlinear calibration curves for COM/COD, COM/HAP, COM/ammonium hydrogen urate, and COM/uric acid mixtures.[5] Estepa fails to provide figures of merit for the calibration curves, but each curve visually deviates from linearity above 50 wt %. Nonlinearity above 50 wt % is most likely attributed to sample thickness and variability as a transmission IR technique was utilized. Additionally, Cohen-Solal's approach required extensive sample preparation including ten cycles of sample grinding and ten cycles of pressing the sample pellet to ensure maximum absorbance with a potassium bromide (KBr) transmission technique. Pellet optimization is emphasized because pellet thickness can affect sample absorbance, but with the use of an ATR technique, measurements are independent of sample thickness. The benefits of ATR over traditional transmission methods include protecting the integrity of delicate samples, significantly reducing sample preparation, and providing better control of experimental parameters necessary for quantitative analysis.[22–24] This research will show that ATR-FTIR can be utilized to produce calibration curves for the quantitative analysis of kidney stone components without extensive sample preparation. Unlike the transmission approach of Cohen-Solal, ATR does not require mixing the sample with an infrared inactive material such as KBr prior to analysis. Grinding and pressing the sample multiple times is not required because ATR measurements are independent of sample thickness provided the sample is thicker than the sampling depth ($3d_p$). Because the measurements are independent of sample thickness, ATR can yield photometrically accurate spectra appropriate for quantitative analysis.

Quantitative ATR-FTIR analysis of solids has been described by Ishida, Iwamoto, and Ohta.[25–27] Recently, ATR has been successfully applied as a quantitative technique for the analysis of pharmaceuticals and polymer films.[28–31] Chen et al. utilized ATR for the

quantitative analysis of polymer blends.[31] Chen reports a calibration curve with a correlation coefficient of 0.9944, proving the quantitative abilities of ATR. In 2003, Helmy et al. analyzed solid pharmaceutical tablets to identify and quantitatively determine the concentration of two drug polymorphs.[30] Helmy reported a detection limit of 3 wt % of one polymorph in the presence of another. Helmy et al. demonstrated the ability of ATR to quantitatively determine small amounts of components in a compact binary sample much like the sample pellets studied in this investigation. The most recent study published in 2006 by Planinšek et al. describes the use of ATR-FTIR for the quantitative analysis of binary pharmaceutical mixtures.[32] Their work resulted in nonlinear calibration curves for several different mixtures of pharmaceutical components. The theory proposed by Planinšek was that the particle sizes of powdered components have an effect on calibration curve linearity. Planinšek explains that a positive deviation from linearity is typically observed for smaller particle fractions and a negative deviation is observed for larger particle fractions. This phenomenon is a result of smaller particles, which occupy a greater specific surface area, surrounding the larger particles, ultimately resulting in a decreased absorbance for the larger particle. Consider a binary mixture of two components with particle sizes of 8 and 140 μm. As the concentration of the larger 140 μm particle increases, there will be larger voids between particles where smaller 8 μm particles can fill in. Planinšek et al. calculated specific surface area (SSA) of each particle as the surface area per unit mass. For example, if two particles have an average size of 8 and 140 μm, the authors report their corresponding SSA values would be 0.17 and 0.08 m^2/g. Therefore, because the smaller particle has a larger SSA, it will experience a larger percentage of interaction with the impinging infrared radiation. With the use of SSA, the authors relied on a two dimensional representation of the surface and did not complete any calculations taking penetration depth into consideration, which is an important aspect of any ATR-FTIR measurement. Planinšek et al. expanded their study further to generate a calibration curve of two large components, which showed linearity. This observation further supported their theory that similar sized components can produce linearity, but small/large particle systems generate nonlinearity. Along with reducing the sample preparation of Cohen-Solal, the current study will also show that linear calibration curves can be generated for small particles of comparable size. Similar to the work by Planinšek, the current work will demonstrate that nonlinearity becomes evident at higher concentrations of the larger particle. Unlike the study by Planinšek, this research will investigate other potential sources of nonlinearity and provide detailed volume calculations, taking penetration depth into account, to support the particle size hypothesis.

This laboratory has been investigating the use of ATR infrared molecular imaging for the analysis of mineral inclusions within biopsied kidney tissue. In 2005, Anderson et al. developed a protocol for the infrared microspectroscopic analysis of mineral inclusions within biopsied tissue that requires the use of a low-e reflective slide.[11] This reflection/absorption approach has revolutionized the way in which small inclusions can be analyzed, but remains qualitative. ATR-FTIR molecular imaging has the potential to quantitatively analyze kidney stone components in conjunction with appropriate calibration curves. ATR-FTIR imaging provides increased spatial resolution allowing the identification of mineral inclusions several micrometers in diameter. Ultimately, the quantitative analysis of small mineral inclusions at the initial stages of stone formation may aid in determining the pathogenesis of idiopathic calcium stone disease. The goal of this research is to investigate ATR as an alternative approach for quantitative kidney stone analysis and identify important factors when using ATR for quantitative studies.

Experimental

Materials and Methods

COM was purchased from Spectrum Chemicals (NJ, USA), HAP was purchased from ACROS organics (NJ, USA) and calcium carbonate ($CaCO_3$) was purchased from EM Science (NJ, USA). Because most stones contain at least two different constituents, samples were analyzed as binary ratios ranging from 0 to 100 wt % COM or HAP. Known amounts of COM and HAP were weighed separately on a Mettler analytical balance to an accuracy of 0.01 mg. The samples were mixed together to obtain 0, 10, 30, 50, 70, 90, and 100 wt % COM. For example, 60.0 mg of HAP was mixed with 140.0 mg of COM to prepare a calibration standard containing 70 wt % COM. The total weights of all calibration standards were kept consistent for each set at 200 mg. To ensure homogeneity, each sample was mixed at ~60 rpm for thirty minutes in an automatic mixer. The mixer, modeled after a large scale V-shaped pharmaceutical mixer, was fabricated with stainless steel tubing and sealed with a Teflon cap. The dimensions of the mixer were determined based on the 200 mg samples utilized and can be seen in Figure 1. Pellets were pressed at 5.0 tons per cm^2 using an SPEX Industries automatic press and an 11 mm pellet die. A minimum of five pellets were pressed and scanned for each concentration.

Instrumentation

Infrared spectra were collected with a Harrick Split-pea ATR microscope interfaced to a Perkin Elmer 2000 Fourier transform infrared spectrometer. This accessory employed a silicon internal reflection element (IRE) and the standard deuterium triglycine sulfate (DTGS) detector on the Spectrum 2000 macro bench. Spectra collected using this device represent the average of 32 individual scans possessing a spectral resolution of 4 cm^{-1}. The samples were brought into intimate contact with the IRE using a loading of 0.5 kg. Spectra were analyzed in absorbance mode. Corrected peak areas, or integrated band intensities, were calculated using Perkin Elmer Spectrum 5.0.1 software and plotted versus concentration (wt %) using a linear regression analysis. Specular reflection measurements were collected with the Perkin Elmer Spotlight 300 infrared microscope interfaced to a Perkin Elmer Spectrum One Fourier transform spectrometer (FTIR). The system employed a 100 × 100 μm liquid nitrogen cooled, mercury cadmium telluride (HgCdTe) detector. Samples were analyzed in the reflectance mode. Spectra collected using this device represent the average of 64 individual scans possessing a spectral resolution of 4 cm^{-1}. Particle size analysis was completed utilizing a Horiba LA-930 analyzer with an automatically aligned, calibrated 87-detector, dual light source optical system. Particle size measurements were collected from 0.02–2000 microns.

Results and Discussion

Cohen-Solal et al. demonstrated the effects of multiple grindings and pressings on sample pellet absorbance.[20] They confirmed that absorbance increases with multiple grindings and pressings of sample pellets and becomes consistent after ten repetitions. Therefore, it was crucial to determine the effect of pressure on absorbance for the pelletized samples employed in this study. To determine an optimum pressure for pellet production, the full width at half maximum was determined for the COM 1620, 1315, and 780 cm^{-1} bands and the 1010 cm^{-1} band of HAP for five pellets pressed at 2.5, 5.0, 7.5 and 10.0 tons per cm^2. Pure samples of COM and HAP were used for these studies. A T-test was calculated for the full width at half maximum (FWHM) values at a 95% confidence level.[33] Statistical overlap was present at 2.5 and 5.0 tons per cm^2. For example, the FWHM for the COM 780 cm^{-1} band was 43.58 ± 0.95 at 2.5 tons and 44.81 ± 1.3 at 5.0 tons, showing overlap between the two values. On the other hand, at 7.5 tons the FWHM increased to 49.89 ± 2.3 and further to

54.89 ± 2.1 at 10 tons. The FWHM for 5 tons no longer overlaps with the value at 7.5 and 10 tons, therefore, 5.0 tons per cm^2 was selected as optimal pressure.

It is apparent that the absorbance of synthetic powders and biological stone samples may not be comparable for several reasons. However, because most natural stones contain more than one component, the choice was made to utilize synthetic COM and HAP powders for the generation of calibration curves. Calibration curves generated with natural materials may not accurately allow quantitation of one component over another if the natural material may be a mixture itself. Further, the main focus of the investigation is to evaluate the feasibility of the ATR method for the quantitative analysis of stone components. Spectra of pure COM, HAP and $CaCO_3$ are shown in Figure 2. The prominent bands used for quantitative analysis include the 1620, 1315, and 780 cm^{-1} bands of COM, the 1010 cm^{-1} band of HAP and the 1400 cm^{-1} band of $CaCO_3$. The detailed assignments for the specified IR bands have previously been reported in the literature and are shortly listed in Table 1.[34–36] Briefly, the 1315 cm^{-1} band of COM corresponds to the symmetric C=O stretch, the asymmetric C=O stretch occurs at 1620 cm^{-1}, and the COM 780 cm^{-1} band is a result of a C-O bend. The 1010 cm^{-1} band of HAP corresponds to the asymmetric υ_3 PO_4^{-3} stretch, and the 1400 cm^{-1} band of $CaCO_3$ is the asymmetric stretch (υ_3) of the carbonate ion. On close inspection, one can observe absorptions located at 1410 and 875 cm^{-1} (out of plane $\upsilon 2$ mode of CO_3^{-}) of the HAP spectrum. These two bands appear in the HAP spectrum as a result of carbonate impurities associated with the manufacturing process. Because the carbonate contaminant was consistent throughout the sample, it should have no effect on the results of the present study. The four COM and HAP bands were chosen for quantitative analysis based on the lack of overlap with bands present in the other component. For example, the 550 cm^{-1} band of HAP was not used for quantitative analysis due to the overlap it experiences with the two bands of COM at ~ 500 and 580 cm^{-1}. Several bands were used for quantitative analysis of COM because if the calibration curves were to be used for the analysis of biopsied tissue with mineral deposits, the amide I band from tissue would overlap with the 1620 cm^{-1} COM band. Therefore, the 1315 and/or 780 cm^{-1} COM bands could be used for quantitation in this case.

When COM integrated bands were utilized for the generation of calibration curves, COM was designated as the analyte and HAP as the matrix (COM/HAP). Likewise, HAP was designated the analyte and COM the matrix (HAP/COM) when the HAP integrated band intensity was plotted. Integrated absorbance values utilized for the calculation of calibration curves were acquired from the same set of standard COM/HAP mixtures. Calibration curves were plotted as integrated band intensity (peak areas) versus weight percent of analyte to matrix. The limits of integration used for quantitative analysis are listed in Table 1. Calibration curves for the 780 cm^{-1} band of COM, and the HAP 1010 cm^{-1} band are shown in Figures 3 and 4. The two figures illustrate curves with the best and worst linear correlation coefficients, respectively. The error bars for each data point along the linear curve represent the standard deviation associated with that set of five corrected peak areas. Table 2 outlines the figures of merit for each component and integrated band. The R^2 values for the four curves show correlation ranging from 0.997 to 0.93.

The limit of detection (LOD) is defined as the minimum amount of analyte that can be detected at a known confidence level. In the present case, LOD was calculated as three times the standard deviation (σ) of the baseline divided by the slope of the calibration curve. Limits of detection for each of the four calibration curves generated range from 0.07 ± 0.02% COM/HAP to 0.26 ± 0.07% HAP/COM. Limit of quantitation (LOQ) is the minimum amount of analyte that can be quantitatively detected by an instrumental method. LOQ was calculated as ten times the standard deviation of the baseline divided by the slope of the calibration curve. Limits of quantitation range from 0.22 ± 0.02% COM/HAP to 0.88 ±

0.07% HAP/COM. The analytical figures of merit show that LOD and LOQ are statistically similar regardless of the band strength. This similarity between the LOD and LOQ for all bands demonstrates that the signal to noise ratio of the measurements is high. The LOD and LOQ uncertainties were calculated as the uncertainty of σ divided by the uncertainty of the calibration curve. Uncertainty of the calibration curve was calculated using equation 1 where s_y is the standard deviation of the integrated band intensity, k is the number of measurements, n is the number of data points, m is the slope of the line, and x and y represent the true and average total value for the data points.[33]

$$s_x = \frac{s_y}{m}\sqrt{\frac{1}{k}+\frac{1}{n}+\frac{(y-\bar{y})^2}{m^2\sum_{i=1}^{n}(x_i-\bar{x})^2}} \quad (1)$$

Despite the acceptable analytical figures of merit for the calibration curves, observation of Figure 4 shows slight nonlinearity around 70 wt %. Previous reports have shown calibration curve nonlinearity for solid state powdered samples utilizing ATR-FTIR including the work by Planinšek discussed earlier.[32,37] Planinšek et al. completed an extensive study of various sized particles where it was determined that particle size and specific surface area play major roles in the distributions of components in a mixture, ultimately affecting the linearity of calibration curves. Their study included calibration curves generated from seven different binary mixtures. The binary mixtures included Mg stearate, methyl orange, Povidone, Eudragit, and stearic acid at various particle sizes. Their first calibration curve attempts involved two binary mixtures of Mg stearate/methyl orange, and Povidone/methyl orange without sieving. The Mg stearate/methyl orange data showed that the smaller particle (Mg stearate) demonstrated positive deviation from linearity and the larger particle showed negative deviation from linearity. The Povidone-methyl orange mixture was considered a mixture of equal sized particles, but also produced positive and negative deviations from linearity. Due to the inconsistent data, the authors produced curves with sieved powdered mixtures. The sieved powders yielded more consistency as a mixture of two large particles (Povidone and Eudragit) produced linear curves. But, when combining sieved mixtures of small and large particles, the smaller particles once again showed positive deviation from linearity and the larger particles showed negative deviations. From this data, it can be concluded that similar sized particles can produce linear data, but due to smaller components occupying a larger specific surface area, mixtures of small and large particles produce nonlinear curves, particularly at higher concentrations.

The present nonlinear calibration curve (Figure 4) is similar to that observed by Planinšek because it drifts from linearity at higher concentrations of the larger particle, but different in that the smaller particles used for this investigation do not show curve nonlinearity. Hopefully, the following considerations will provide a clarified explanation for the nonlinearity so commonly encountered with solid state ATR-FTIR quantitative analysis. For ATR-FTIR there are several parameters that could be responsible for the nonlinearity observed in Figure 4. These parameters include refractive index, penetration depth, and particle size. Initially, the refractive indices of COM and HAP were determined by collecting specular reflection measurements from polished crystals of the minerals (Excalibur Mineral, NY). Perkin Elmer Spectrum 5.0.1 software was used to conduct a Kramers Kronig transformation on the specular reflection spectra. The n-index spectrum was calculated and the refractive index values were averaged over each band used for quantitation. The refractive indices of HAP and COM were measured to be 1.82 and 1.92 respectively. Next, penetration depth was calculated using the following equation:

$$d_p = \frac{\lambda_0}{2\pi \cdot n_c\left(\sin^2\Theta - \left(\frac{n_s}{n_c}\right)^2\right)^{1/2}} \quad (2)$$

where n_s and n_c are the refractive indices of the sample and crystal respectively.[23] If n_s=1.82 and n_c=3.41 (silicon IRE), the depth of penetration for the HAP 1010 cm^{-1} band is 0.99 μm. Therefore, the sampling depth ($3d_p$) is 2.97 μm. Penetration depth calculations were solved for mixtures of HAP and COM from 0–100%. For example, a 70% HAP/COM sample would have a weighted average refractive index of 1.85, resulting in a penetration depth of 1.02 μm and a sampling depth of 3.06 μm. Next, the penetration depth values were plotted against weight percent producing a linear correlation coefficient of 0.9985. This linear relationship between penetration depth and concentration shows that penetration depth is not a contributing factor to nonlinearity.

To investigate other potential sources of calibration curve nonlinearity, instrumental, sample, and sample preparation errors were calculated as relative standard deviation (RSD). Errors were determined by taking the corrected peak area of the COM 736–800 cm^{-1} band at 70% HAP/COM. The 70% HAP/COM ratio was chosen because curve nonlinearity becomes evident at this point. First, instrumental error was calculated by collecting five scans at the same location on one pellet. Instrumental error shows the least effect on curve linearity with an RSD of 2.2%. Next, sample preparation error was determined by scanning five pellets which were all prepared in the same manner. Sample preparation also has little effect on linearity with an RSD of 8.1%. Finally, sample error was determined by collecting five scans at different locations on one pellet. Sample error proved to be the most influential source of error with an RSD of 20%. Ultimately, the instrumental, sample and sample preparation errors do not provide conclusive evidence for the predominant source of nonlinearity.

Because all indications are that particle size variability contributes to the nonlinearity in Figure 4, the particle sizes of HAP and COM were measured with a particle size analyzer to be 76 and 20 μm respectively. Planinšek et al. used specific surface area, or surface area per unit mass (m^2/g), for the calculations in their study. For the current study, volume (μm^3) was chosen because once penetration depth is taken into account; the ATR sampling method involves three dimensions. Only recently solved mathematically, the Kepler conjecture describes the issue of optimally packing equal sized spheres into a cube.[38] The conjecture explains that hexagonal close packed and face centered cubic packed arrangements of equal sized spheres produce the highest possible packing density. With the hexagonal close packed arrangement, the volume occupied by equal sized spheres in a cube is approximately 74%. Therefore, depending on the ratio of a powdered mixture, 26% of the cube is void space which could be occupied by smaller particles. For the current study, the situation does not involve packing spheres in a cube, but rather one layer of spheres packed tightly in a 200 × 200 × 76 μm volume. Figure 5 illustrates this situation. If HAP particles of 76 μm are hexagonal close packed in the 200 × 200 μm IRE sensing area, the volume occupied by the spheres is calculated to be approximately 87%. For a 100% HAP sample pellet, there would be 13% void space. The void space would ultimately lead to less IRE contact with the sample resulting in decreased absorbance for the samples containing higher concentrations of HAP. However, Figure 5 of the current study does not completely demonstrate the current situation because in actuality the infrared radiation only penetrates into the sample to $3d_p$. Therefore, the diameter of the spheres sensed by the infrared radiation is actually 28 μm (white shaded area of Figure 5) for each 76 μm particle. In this case, approximately 10% volume is occupied by the spheres. So in actuality, for a 100% HAP sample, there is the potential to have up to 90% void space leading to less IRE contact with the sample and a

decreased absorbance. A decreased absorbance at higher concentrations of HAP would lead to the negative deviations observed in Figure 4. Planinšek et al. utilized larger particles than the current study (up to 158 μm), but they also utilized a 2 mm diamond ATR crystal. Therefore, due to the larger sampling volume, linearity can still be achieved with mixtures of two large components (116 and 110 μm) as shown in their Figure 6.[32] Furthermore, it should be noted that the current calculations do not take into account the compressibility of the particles. As the powdered samples are pressed into the confined area of the pellet die, there will be a certain amount of compression experienced by the particles, which is not easily determined.

Because the compressibility of the particles is unknown, scanning electron microscopy (SEM) images were collected to visibly observe the surface topography of the sample pellets. Planinšek et al. conducted a similar study, but used colored particle mixtures and observed the color distribution with an optical microscope.[32] They mixed methyl orange (158 μm) with Povidone (140 μm) for a large-large particle sample and methyl orange (158 um) with Mg Stearate (8 μm) for a large-small particle sample in a 1:1 ratio. After visual observation, the authors noted that there were a higher number of small size components on the mixture surface, confirming their theory that smaller particles fill in more void space and experience a larger specific surface area. SEM was chosen for the current study because a more detailed observation of the sample surface was desired. The 90% and 10% HAP sample pellets were imaged because higher concentrations of HAP produce the nonlinearity evident in Figure 4. As illustrated in Figures 6 and 7, the visible data shows that the 90% HAP sample has voids with ~0.5 to 1 μm spaces between particles, which would ultimately lead to less IRE contact with the sample. A decrease in this contact would result in reduced absorbance for HAP at higher HAP concentrations. The 10% HAP sample pellet has a much smoother surface, without voids, which would ultimately lead to a greater IRE surface coverage and increased absorbance for the smaller particles.

To verify that particle size is the cause of calibration curve nonlinearity, an additional calibration curve was generated utilizing calcium carbonate ($CaCO_3$) and COM. $CaCO_3$ is another kidney stone component similar in size to COM whose average particle size was measured with a particle size analyzer to be 29 μm (COM particle size is 20 μm). The calibration curve for the 1400 cm^{-1} carbonate band of $CaCO_3$ is shown in Figure 8. The limits of integration used for calculating the calibration curve were 1350–1440 cm^{-1}. The carbonate band was chosen for integration because it is a well known strongly absorbing band, much like the phosphate band of HAP. The data presented in Figure 8 shows linearity is evident and the curve does not deviate from linearity above 70 weight %. Therefore, one can conclude that linear curves can be obtained for mixtures of particles with similar size provided the particles are considerably smaller than the IRE sampling area (in this case, 200 μm). In the present case, the particle size should be approximately 8 times smaller than the IRE sampling area.

For the application of the proposed method for kidney biopsy analysis, the particle sizes of mineral inclusions have to be considered relative to the IRE sample area. For a 6 μm wavelength, the diffraction limited sampling area in an ATR microscopic measurement is 6 μm in diameter. The sizes of mineral inclusions are certainly in this range and can be larger meaning that the IRE sampling area is filled. With regard to the particle sizes in mineral inclusions, it has been reported that particles of Randall's plaque in biopsies taken from kidneys of patients with calcium oxalate stones can range in size from 0.05 to 0.4 μm in diameter.[39] Considering the small nature of natural stone particles, it is anticipated that reproducible quantitation could be achieved with the reported calibration curves.

Conclusion

A new quantitative approach requiring minimal sample preparation for kidney stone analysis (ATR-FTIR) has been realized. It has been shown that linear calibration curves can be obtained provided the system is well understood with regard to particle size. Linearity can be achieved if the particle sizes of the two materials are comparable and considerably less than the IRE sampling area. In this study, particles on the order of 20–29 μm produced linear calibration curves with an IRE sampling area of 200 × 200 μm. Furthermore, calibration curves that included particles as large as 76 μm produced a drift in linearity at higher concentrations of the larger particle. With careful consideration of natural stone particle size, ATR-FTIR microspectroscopic imaging for the quantitative analysis of mineral inclusions within biopsied kidney tissue should be feasible.

Acknowledgments

The authors would like to thank James Williams of Indiana University Medical School for the natural stone samples and insight into natural stone particle sizes. Also, thanks to Barry Landrum of the instrumentation shop at Miami University for fabrication of the mixer and Matt Duley of the scanning electron microscopy laboratory at Miami University for the SEM images.

References

1. Stamatelou KK, Francis ME, Jones CA, Nyberg LM, Curhan GC. Kidney Int. 2003; 63:1817. [PubMed: 12675858]
2. Kasidas GP, Samuell CT, Weir TB. Ann Clin Biochem. 2004; 41:91. [PubMed: 15025798]
3. Pearle MS, Calhoun EA, Curhan GC. J Urol. 2005; 173:848. [PubMed: 15711292]
4. Clark JY, Thompson IM, Openberg SA. The Journal of Urology. 1995; 154:2020. [PubMed: 7500448]
5. Estepa L, Daudon M. Biospectroscopy. 1997; 3:347–369.
6. Maurice-Estepa L, Levillain P, Lacour B, Daudon M. Clin Chim Acta. 2000; 298:1–11. [PubMed: 10876000]
7. Coe FL, Parks JH. Hosp Pract (Off Ed). 1988; 23:185. [PubMed: 3126203]
8. Khan SR. Urol Res. 2006; 34:86–91. [PubMed: 16404622]
9. Khan SR, Kok DJ. Frontiers in Bioscience. 2004; 9:1450–1482. [PubMed: 14977559]
10. Khan SR, Glenton PA. J Urol. 1995; 153:811. [PubMed: 7861545]
11. Anderson J, Dellomo J, Sommer A, Evan A, Bledsoe S. Urol Res. 2005; 33:213. [PubMed: 15703966]
12. Evan AP, Coe FL, Lingeman JE, Shao Y, Sommer AJ, Bledsoe SB, Anderson JC, Worcester EM. Anat Rec. 2007; 290:1315.
13. Evan A, Lingeman J, Coe FL, Worcester E. Kidney Int. 2006; 69:1313. [PubMed: 16614720]
14. Evan AP, Lingeman JE, Coe FL, Parks JH, Bledsoe SB, Shao Y, Sommer AJ, Paterson RF, Kuo RL, Grynpas M. J Clin Invest. 2003; 111:607. [PubMed: 12618515]
15. Khand FD, Ansari AF, Khand TU, Memon JM. Jour Chem Soc Pak. 1996; 18:246–249.
16. Gault MH, Ahmed M, Kalra J, Senciall I, Cohen W, Churchill D. Clin Chim Acta. 1980; 104:349–359. [PubMed: 7389143]
17. Sutor, DJ. Urinary Stones: Clinical and Laboratory Aspects. Lancaster: MTP Press; 1982. X-Ray Diffraction Analysis of Urinary Calculi; p. 107-133.
18. Medina, JA. Renal Tract Stone Metabolic Basis and Clinical Practice. Churchill Livingstone; London: 1990. Scanning Electron Microscopy of Urinary Stones; p. 39-44.
19. Rose GA, Woodfine C. Br J Urol. 1976; 48:403–412. [PubMed: 1009320]
20. Cohen-Solal F, Dabrowsky B, Boulou JC, Lacour B, Daudon M. Appl Spectrosc. 2004; 58:64–67.
21. Volmer M, Bolck A, Wolthers BG, de Ruiter AJ, Doornbos DA, van der Silk W. Clin Chem. 1993; 39:948–954. [PubMed: 8504562]

22. Chalmers JM, Griffiths PR. Handbook of Vibrational Spectroscopy. 2002; 2:933–959.
23. Harrick, NJ. Internal Reflection Spectroscopy. Interscience; New York: 1967.
24. Harrick NJ. Phys Rev Lett. 1960; 4:224.
25. Ishida H. Rubber Chem Technol. 1987; 60:497.
26. Iwamoto R, Ohta K. Appl Spectrosc. 1984; 38:359.
27. Ohta K, Iwamoto R. Appl Spectrosc. 1985; 39:418.
28. Kirov KR, Assender HE. Macromolecules. 2004; 37:894.
29. Kirov KR, Assender HE. Macromolecules. 2005; 38:9258.
30. Helmy R, Zhou GX, Chen YW, Crocker L, Wang T, Wenslow RM Jr, Vailaya A. Anal Chem. 2003; 75:605. [PubMed: 12585491]
31. Chen J, Gardella JA Jr. Appl Spectrosc. 1998; 52:361.
32. Planinsek O, Planinsek D, Zega A, Breznik M, Srcic S. Int J Pharm. 2006; 319:13. [PubMed: 16730933]
33. Harris, DC. Quantitative Chemical Analysis. W.H. Freeman and Co; New York: 2007.
34. Shippey TA. J Mol Struct. 1980; 63:157.
35. Petrov I, Soptrajanov B. Spectrochim Acta, Part A. 1975; 31A:309.
36. Fowler BO. Inorg Chem. 1974; 13:194.
37. Anderson, JC. PhD Dissertation. Miami University; Oxford, OH: 2007.
38. Szpiro, GG. Kepler's Conjecture. Wiley, John & Sons Inc; 2003.
39. Ryall RL. Urol Res. 2008; 36:77. [PubMed: 18286270]

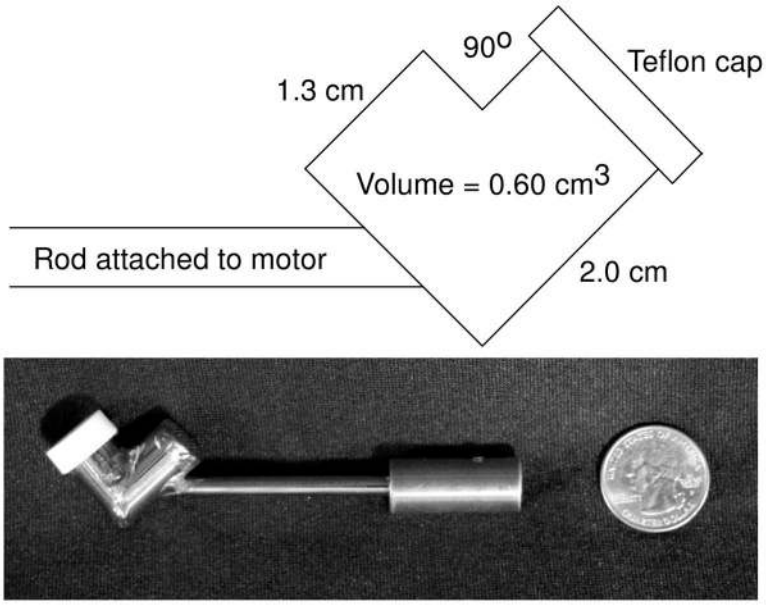

Figure 1.
Dimensions of fabricated automatic mixer used to eliminate sample variability.

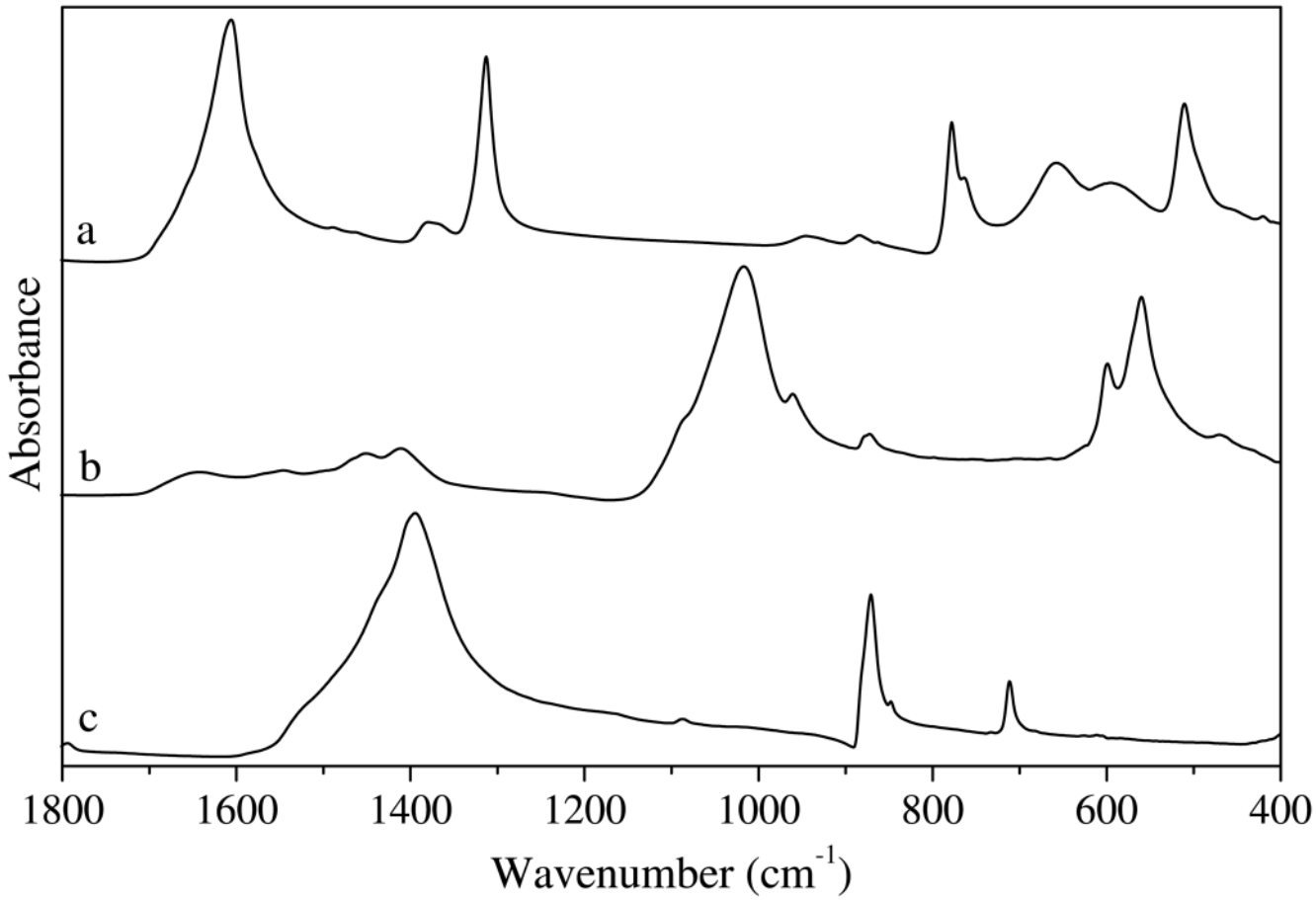

Figure 2.
Pure spectra of COM (a), HAP (b) and $CaCO_3$ (c).

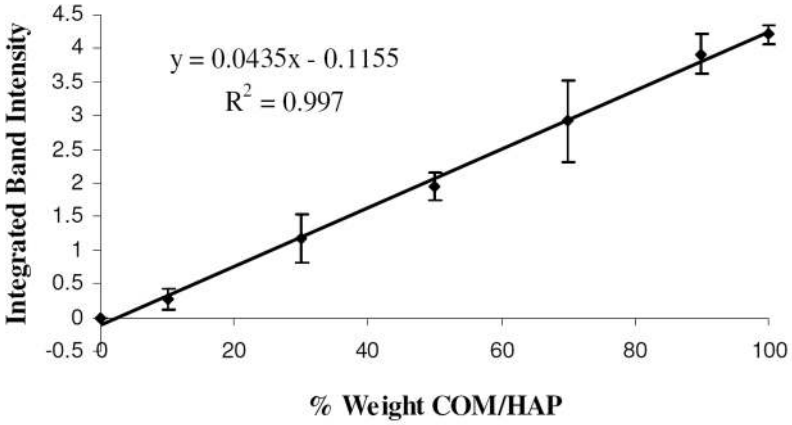

Figure 3.
Calibration curve for the COM 780 cm^{-1} band.

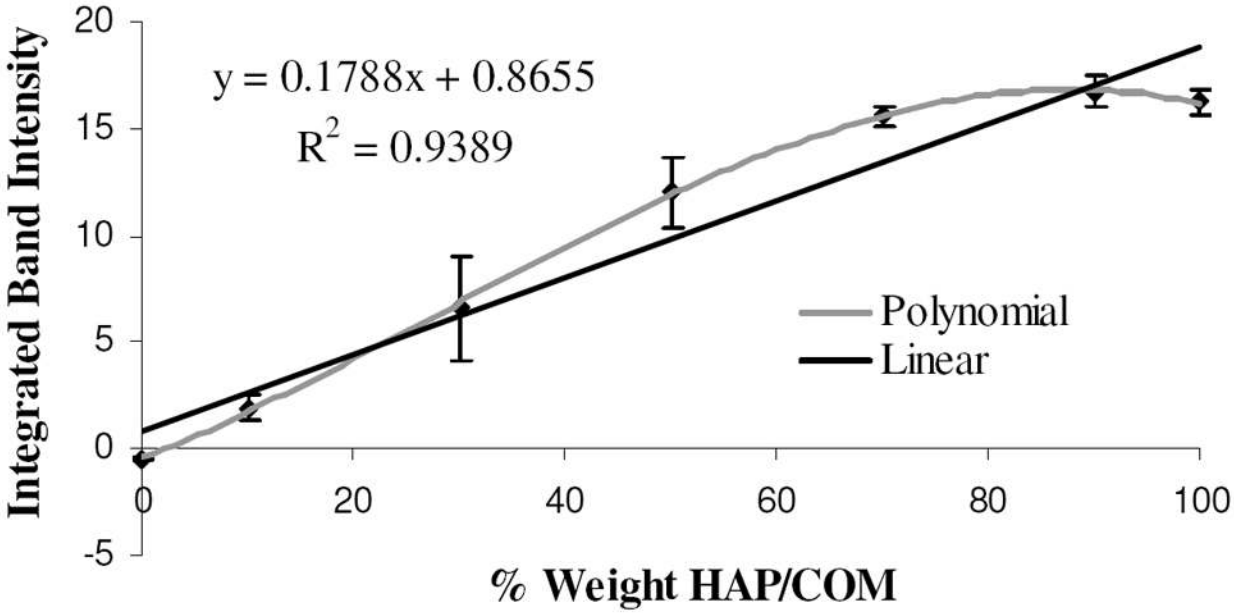

Figure 4.
Calibration curve for the HAP 1010 cm^{-1} band.

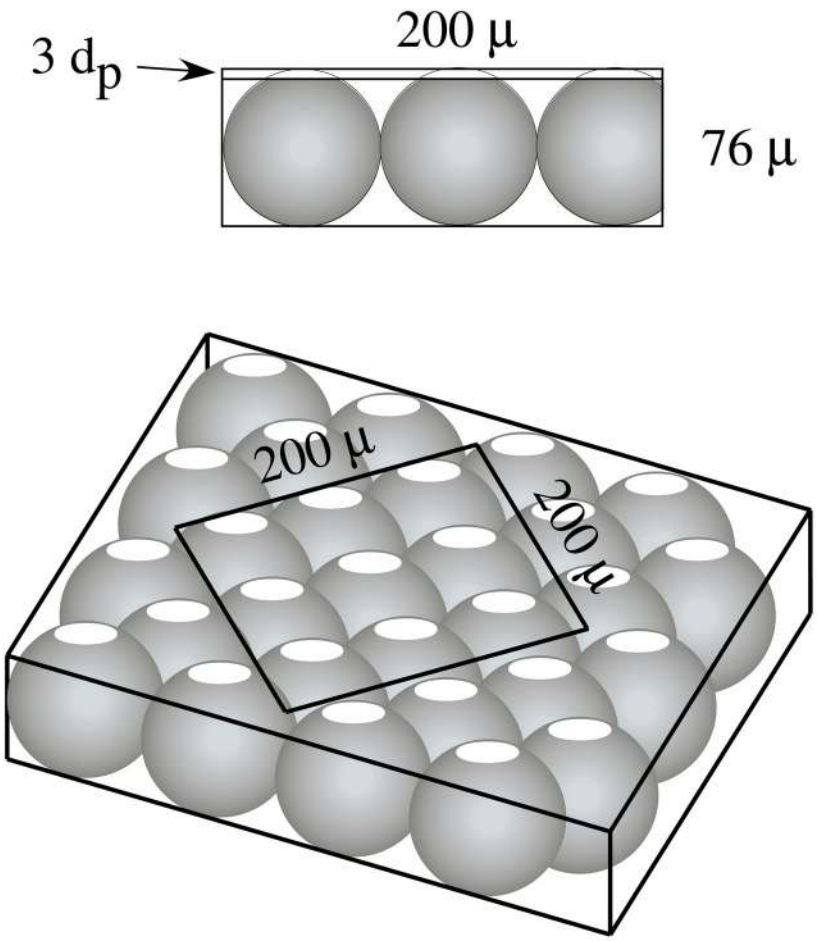

Figure 5.
Schematic of the 76 μm HAP particles in a hexagonal close packed arrangement corresponding to an ~87% volume fill. There is an apparent size of 28 μm (white shaded area) because the infrared radiation only samples $3d_p$ of the 76 μm HAP particles corresponding to an ~10 % volume fill.

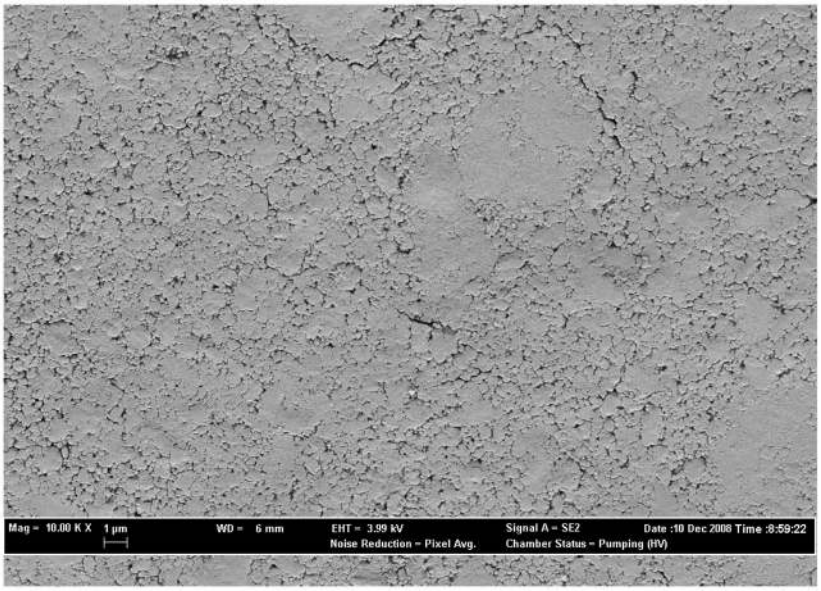

Figure 6.
SEM image of the 90% HAP/COM pellet. Surface shows ~0.5–1 μm voids between particles which would lead to less IRE contact with the sample resulting in decreased absorbance at higher concentrations of HAP.

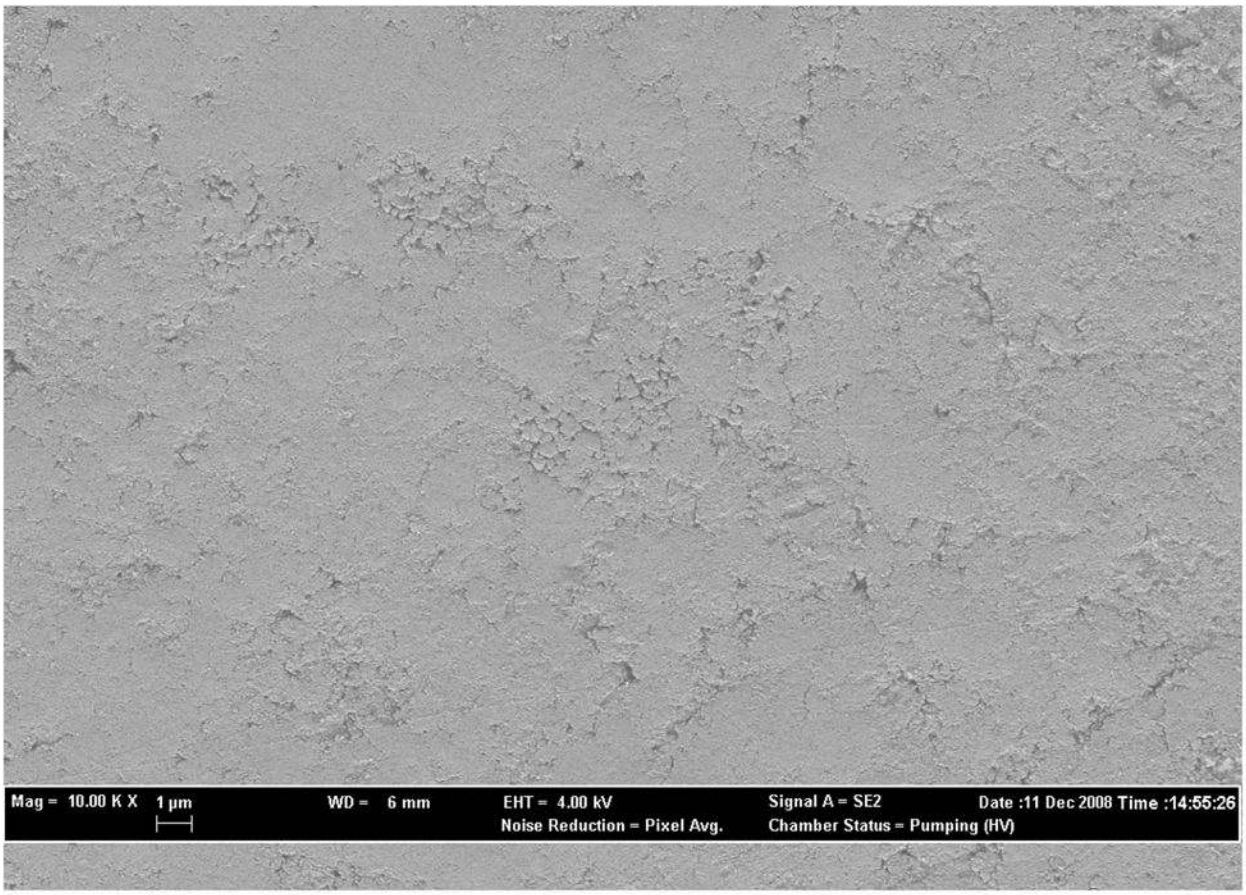

Figure 7.
SEM image of the 10% HAP/COM pellet. Surface appears more uniform, or fewer voids than Figure 6, leading to greater IRE surface coverage resulting in increased absorbance at lower concentrations of HAP.

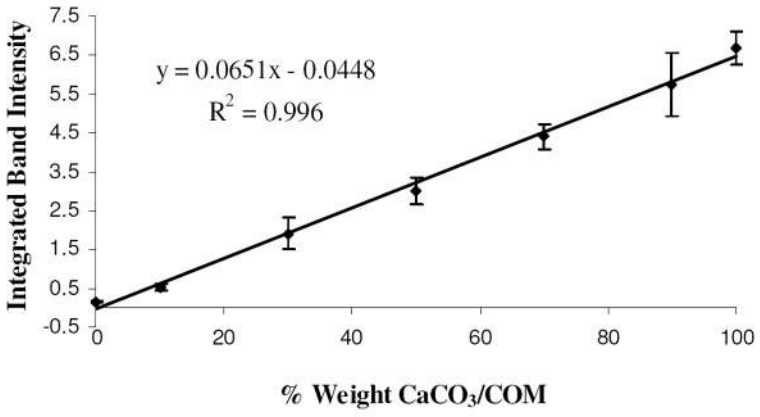

Figure 8.
Calibration curve for the $CaCO_3$ 1400 cm^{-1} band.

Table I

IR bands, assignments, and limits of integration utilized for quantitative analysis

Component / band	Assignment	Limit of Integration
COM 1315 cm^{-1}	υ_s C=O stretch	1266–1346 cm^{-1}
COM 1620 cm^{-1}	υ_{as} C=O stretch	1498–1700 cm^{-1}
COM 780 cm^{-1}	C-O bend	736–800 cm^{-1}
HAP 1010 cm^{-1}	υ_{as} PO_4^{-3} stretch	968–1146 cm^{-1}
$CaCO_3$ 1400 cm^{-1}	υ_{as} C=O stretch	1350–1440 cm^{-1}

Table II

Analytical figures of merit for the calibration curves

Component/Band	Slope (abs/%wt)	Y-Intercept (abs)	R^2	LOD	LOQ
COM 1315 cm^{-1}	0.0656	−0.3636	0.9925	0.11 ± 0.03%[a]	0.37 ± 0.03%[a]
COM 1620 cm^{-1}	0.2277	0.2744	0.9931	0.07 ± 0.02%[a]	0.22 ± 0.02%[a]
COM 780 cm^{-1}	0.0435	−0.1155	0.9975	0.09 ± 0.03%[a]	0.29 ± 0.03%[a]
HAP 1010 cm^{-1}	0.1788	0.8655	0.9389	0.26 ± 0.07%[b]	0.88 ± 0.07%[b]

[a] % COM/HAP

[b] % HAP/COM

Appl Spectrosc. Author manuscript; available in PMC 2012 March 21.